mater.scichina.com link.springer.com

Published online 30 May 2023 | https://doi.org/10.1007/s40843-023-2443-0
Sci China Mater 2023, 66(8): 3165–3175

Facile synthesis of a Z-scheme CeO_2/C_3N_4 heterojunction with enhanced charge transfer for CO_2 photoreduction

Jie Chen[1], Yuting Xiao[2], Nan Wang[1], Xin Kang[1], Dongxu Wang[1], Chunyan Wang[1], Jiancong Liu[1*], Yuchen Jiang[1] and Honggang Fu[1*]

ABSTRACT **Using solar energy to convert CO_2 into value-added fuel is crucial for the goal of global carbon neutrality. Effective separation of photogenerated charges is important for improving photocatalytic CO_2 reduction efficiency. Herein, we report a facile *in situ* exfoliation and conversion strategy to synthesize a novel CeO_2/C_3N_4 heterostructure by uniformly distributing CeO_2 nanoparticles onto ultrathin porous C_3N_4 nanosheets. The ultrathin porous structure of C_3N_4 not only increases the specific surface area to provide more active sites but also effectively shortens the migration distance of photogenerated electron holes to avoid their recombination. In addition, the well-dispersed CeO_2 on C_3N_4 shows an intimate interface contact, which allows more charges to be transferred through the increased interface surface area. The as-synthesized CeO_2/C_3N_4 heterojunction with well-matched band gaps and a Z-scheme structure prolongs the lifetime of photoinduced charge carriers and maximizes the redox ability of the photocatalyst. Without a noble metal cocatalyst or a sacrificial agent, the CO_2 photoreduction performance of the CeO_2/C_3N_4 heterojunction is approximately 5-fold enhanced compared with that of bulk C_3N_4. This study provides a facile strategy for the design and practical application of direct Z-scheme photocatalysts for sustainable energy conversion.**

Keywords: Z-scheme heterojunction, CeO_2/C_3N_4, photocatalysis, CO_2 reduction

INTRODUCTION

Converting CO_2 into value-added chemical fuels is crucial for the energy crisis and environmental pollution problems induced by the greenhouse effect [1–4]. Photocatalytic CO_2 conversion can not only reduce the total CO_2 concentration but also obtain useful chemical materials, which is considered one of the most sustainable and greenest strategies for achieving global carbon neutralization [5–9]. Developing novel photocatalysts with a high solar energy utilization rate and a high CO_2 conversion rate is of great importance.

Recently, carbon nitride (C_3N_4) has been considered a promising photocatalyst for CO_2 photoreduction owing to its low cost, metal-free nature, robustness, environmental friendliness, and appropriate band gap [10–12]. However, the inherent defects of C_3N_4 always induce fast electron-hole recombination, which seriously affects its photocatalytic performance. Strategies must be carried out to facilitate the electron-hole separation. Notably, compared with bulk C_3N_4 (BCN), two-dimensional (2D) C_3N_4 nanosheets have a larger specific surface area and faster electron transfer rate, which facilitates the photoinduced carrier migration to the surface and suppresses the recombination of electrons and holes, thereby improving the efficiency of solar energy conversion [13–15]. Moreover, designing an effective heterojunction with a suitable energy band structure is another method to enhance the charge separation efficiency, suppress the recombination of electrons and holes, and facilitate photocatalytic performance [16–18]. First, materials with overlapping band structures with C_3N_4 should be selected to build reasonable heterojunctions to ensure the mutual transfer of photoinduced electrons and holes [19]. Second, it is beneficial to adjust the geometric dimensionality and morphology of photocatalysis nanomaterials to expand the specific surface area, increase the surface active sites, and promote charge transfer [20–22]. Third, maximizing and optimizing the contact interface between the two semiconductors effectively expedite the charge transfer rate and improve their photocatalytic performance. Thus far, methods such as self-assembly under heat treatment [23] and mechanical stirring [24], which are used to synthesize the two semiconductors separately before preparing the composite catalysts, have been developed to synthesize C_3N_4-based heterojunctions. Recently, *in situ* methods such as one-step solvothermal phosphating [25], co-calcination [26], and chemical precipitation [27] have been developed to synthesize C_3N_4-based heterojunctions with a more intimate contact for improved charge transfer. Therefore, designing proper *in situ* methods to construct semiconductor nanoparticles onto 2D C_3N_4 nanosheets by matching the band gaps and controlling intimate contact can further promote the electron-hole separation and improve their photocatalytic properties.

Inspired by natural photosynthesis, constructing an artificial Z-scheme photocatalyst is considered a promising strategy for CO_2 reduction because of its spatially separated active sites for reduction and oxidation and strong redox ability [28]. Generally, a Z-scheme heterojunction is composed of a reduction semiconductor with a negative conduction band (CB) and an oxidation semiconductor with a positive valence band (VB). Under light excitation, the electrons are excited from the VBs of the two semiconductors to the CBs, leaving photoinduced holes in the VBs. Then, the photoexcited electrons in the oxidative semiconductor directly migrate and recombine with the photo-

[1] Key Laboratory of Functional Inorganic Material Chemistry, Ministry of Education, Heilongjiang University, Harbin 150080, China
[2] Key Laboratory of Jiangxi Province for Persistent Pollutants Control and Resources Recycle, Nanchang Hangkong University, Nanchang 330063, China
* Corresponding authors (emails: jiancong@gmail.com (Liu J); fuhg@vip.sina.com (Fu H))

induced holes in the reductive semiconductor [29]. In this way, the separation of reductive and oxidative active sites can be further promoted. Simultaneously, the redox ability of the Z-scheme heterojunction can be efficiently enhanced [30]. Therefore, the design and manufacture of new Z-scheme heterostructure nanocomposites with appropriate band positions and improved charge separation and transfer are needed to improve photocatalytic efficiency. C_3N_4 can easily form heterojunctions with various semiconductor materials for its negative CB, narrow bandgap, and ideal physical/chemical properties. To construct an efficient C_3N_4-based Z-scheme photocatalyst, choosing another semiconductor with a more positive VB position and matched bandgap is the key issue for achieving improved directional electron transfer.

Cerium dioxide (CeO_2), a commonly used oxide semiconductor material, has the advantages of a positive VB position, abundant surface defects, and controllable morphology [31]. Interestingly, Ce^{3+} and Ce^{4+} can coexist on the CeO_2 surface. Oxygen vacancies (V_O) are generated based on the redox behavior between Ce^{4+} and Ce^{3+}, which can act as active sites for CO_2 adsorption and photocatalytic reduction [32]. In addition, the V_O and Ce^{3+} benefit the formation of defect energy levels under the CB of CeO_2, which can narrow the bandgap of CeO_2 and enhance the visible light absorption efficiency. Further, the narrowed bandgap of CeO_2 is near the bandgap of C_3N_4, which can produce similar amounts of photogenerated electrons and holes under irradiation and promote electron transfer from the CB of CeO_2 to the VB of C_3N_4, forming a Z-scheme heterojunction. Furthermore, catalysts with small sizes often induce larger specific surface areas and an increased amount of surface active sites, which is more conducive to the occurrence of adsorption and chemical reactions. Therefore, constructing a novel heterojunction structure with small-sized CeO_2 particles uniformly distributed on C_3N_4 nanosheets can achieve proper Z-scheme heterostructures with not only effective contact and well-matched band structures to promote electron-hole separation but also a large specific surface area with multiple active sites and enhanced CO_2 adsorption.

Herein, using an *in situ* exfoliation and conversion strategy, we have successfully fabricated a CeO_2/C_3N_4 heterojunction with increased specific surface area, promoted photogenerated carrier separation, enhanced CO_2 adsorption, and high CO_2 photoreduction activity. The C_3N_4 nanosheets feature a nanoporous structure with enhanced surface area. Further, CeO_2 nanoparticles are uniformly distributed on the nanosheets, with an average particle size of 18.8 nm. The obtained CeO_2/C_3N_4 heterojunction possesses a direct Z-scheme structure, which enables semiconductors to facilitate the separation of photogenerated charges and maintain the redox capacity at the appropriate position for photochemical CO_2 reduction. The intimate interface between CeO_2 and C_3N_4 also enables more charges to be transferred because of the increased surface area, which leads to an increased rate of CO_2 photoreduction. Benefiting from the increased specific surface area, promoted photogenerated carrier separation, and enhanced CO_2 adsorption, the obtained CeO_2/C_3N_4 heterojunction shows CO and CH_4 yields of 35.96 and 2.40 μmol g^{-1}, respectively, for 4 h without a noble metal cocatalyst or a sacrificial agent, which are much higher than those of BCN, CeO_2, and CeO_2/BCN. This study provides a springboard for the design and practical application of ultrathin C_3N_4-based direct Z-scheme photocatalysts.

EXPERIMENTAL SECTION

Synthesis of CeO_2/C_3N_4 composites

The CeO_2/C_3N_4 composites were synthesized using an *in situ* exfoliation and conversion approach. First, the hexagonal rod-like layered precursor was prepared according to our previously reported method [33]. Typically, 1 g of melamine was mixed with 1.2 g of phosphorous acid and 100 mL of deionized water in a beaker, and then the beaker was placed in a water bath at 80°C for 1 h under vigorous stirring. Second, the solution was transferred to a Teflon-lined autoclave and treated at 180°C for 10 h. After naturally cooling to room temperature, the precursors were obtained by washing the obtained solid with deionized water repeatedly and drying at 60°C. Third, 0.8 g of the precursor was placed in a two-necked flask connected with a funnel and a circulating water vacuum pump, which was used to remove the air in the flask and adsorbed in the precursors as much as possible to reach high vacuum (vacuum degree: −0.1 MPa). Fourth, 0.4 g of $Ce(NO_3)_3{\cdot}6H_2O$ was dissolved in a mixed solvent of 10 mL of ethanol and 3 mL of ethylene glycol. This solution was added to the flask through a funnel with continuous stirring under a vacuum. After continuous stirring for 30 min, the solid was collected by centrifugation to remove the cerium ions, which were not inserted into the interlayer of the precursors, and then the precipitate was redissolved in a mixed solution of 15 mL of ethanol and 5 mL of ethylene glycol. Finally, the mixture was hydrothermally heated at 180°C for 30 min, followed by cooling to room temperature naturally. The obtained solid was washed three times with ethanol, then dried at 60°C overnight, and finally calcined at 440°C for 4 h in a muffle furnace. The product was labeled as CeO_2/C_3N_4.

Synthesis of BCN

BCN was obtained by directly heating urea in a covered crucible at 550°C for 3 h at a heating rate of 2°C min^{-1}.

Synthesis of CeO_2/BCN composites

For comparison, CeO_2/BCN was synthesized using BCN as the matrix rather than a layered precursor. This method is similar to the synthesis of CeO_2/C_3N_4. BCN and $Ce(NO_3)_3{\cdot}6H_2O$ were mixed in 15 mL of ethanol and 5 mL of ethylene glycol under stirring for 30 min and hydrothermally reacted at 180°C for 30 min. Then, the obtained precipitate was washed with ethanol, dried, and finally calcinated in air at 440°C for 4 h.

Synthesis of CeO_2

Briefly, 0.1 g of $Ce(NO_3)_3{\cdot}6H_2O$ was dissolved in 20 mL of ethanol with magnetic stirring for approximately 30 min. Afterward, the solution was transferred to a 50-mL Teflon-lined autoclave and heated for 10 h at 180°C, followed by naturally cooling in air. The solid products were collected by centrifugation, washed with ethanol, and dried at 60°C. Finally, the samples were calcined in air at 440°C for 4 h.

Characterization

The surface morphology and particle size of samples were obtained using scanning electron microscopy (SEM, Hitachi S-4800) with an acceleration voltage of 5 kV and transmission electron microscopy (TEM, JEOL F200) at 200 kV. Powder X-ray diffraction (XRD) patterns were obtained from a Bruker D8 Advance diffractometer with Cu Kα radiation (λ = 1.5406 Å). N_2

adsorption-desorption isotherms were measured by Micromeritics Tristar II. X-ray photoelectron spectroscopy (XPS) and VB XPS spectra measurements were performed on a VG ESCALABMK II with Mg Kα achromatic X-ray source. The ultraviolet-visible (UV-Vis) diffuse reflectance spectrum (DRS) was obtained from a Shimadzu UV-2550. Photoluminescence (PL) spectra were obtained from a Hitachi F-4600 fluorescence spectrophotometer with a photoexcitation wavelength of 365 nm. Fourier transform infrared (FT-IR) spectroscopy was recorded on a Nicolet iS 50 FT-IR spectrometer, using KBr as the diluent. Electron paramagnetic resonance (EPR) measurements were performed on a Bruker EMX plus model spectrometer. *In situ* diffuse reflectance infrared Fourier transform (*in situ* DRIFT) spectra were recorded on a Nicolet iS 50 FT-IR spectrometer using a DRIFT cell with a quartz window. Before the test, the photocatalyst was placed in an *in situ* chamber and purged with Ar for 60 min to remove impurities adsorbed on its surface. Then, high-purity CO_2 was bubbled into deionized water, and the mixture of CO_2 and water vapor was introduced for 30 min. Finally, the DRIFT spectra were recorded under different illumination times. The thickness of the sample was analyzed using a Multimode Nanoscope VIII instrument (Bruker) atomic force microscope (AFM). Thermogravimetric analysis (TG) was performed on a TA Q600 thermal analyzer at a heating rate of 5°C min^{-1}. The work functions were measured using a scanning Kelvin probe (SKP5050, Scotland).

Photochemical measurements

The photochemical tests of the samples were performed in a conventional three-electrode quartz cell using a computer-controlled CHI660E electrochemical workstation. The light source was a 300-W Xe lamp with a simulated sunlight filter (AM 1.5). An Ag/AgCl electrode and a platinum wire were used as the reference electrode and the counter electrode, respectively. A Na_2SO_4 solution (0.2 mol L^{-1}) was used as the electrolyte after nitrogen was injected for 3 h. The process to prepare the working electrode with the as-obtained sample was as follows: 10 mg of catalyst was dispersed in 2 mL of ethanol. After ultrasonic treatment, the obtained homogeneous suspension was sprayed on the surface of fluorine-doped tin oxide glass with an area of 1 cm^2 and calcined at 350°C for 2 h in a nitrogen atmosphere for further use.

Photocatalytic activity for the reduction of CO_2

The photocatalytic CO_2 reduction performance of the catalysts was evaluated using a Labsolar-6A (Beijing Perfectlight) online test device. The photocatalyst (10 mg) and 3 mL of H_2O were added to the reaction vessel, which was evacuated to remove air and then filled with CO_2 (> 99.999%) until the pressure was 80 kPa. After the reactor was maintained for 30 min to establish adsorption-desorption equilibrium, a 300-W xenon lamp (Beijing PerfectLight) was used as the light source. No cocatalysts or sacrificial agents were used during the photocatalytic reaction. The photocatalytic reactor was connected to an online gas chromatograph for hourly gas collection and analysis. Gas products were analyzed using a gas chromatograph (GC 2002, Shimadzu) equipped with a flame ionization detector and a thermal conductivity detector.

Theoretical calculations

All calculations were implemented by the Vienna *Ab-initio* Simulation Package code [34]. The generalized gradient approximation Perdew-Burke-Ernzerhof functional was selected for the exchange and correlation potential [35]. Weak van der Waals interaction was considered by the density functional theory (DFT)-D3 functional [36]. The cut-off energy for the plane wave was 400 eV. The gamma point in the Brillouin zone was chosen for integration. The total energies of the systems converged to 10^{-5} eV in the iterative solution to the Kohn-Sham equation. The force on each atom was reduced to 0.05 eV $Å^{-1}$ after geometry optimization.

RESULTS AND DISCUSSION

Morphological and structural information

An *in situ* exfoliation and conversion method was used to synthesize the CeO_2/C_3N_4 composites (Fig. 1a). First, layered supramolecular precursors were synthesized by the hydrothermal method. Second, ethanol and ethylene glycol helped cerium ions to insert into the interlayer of the precursor under vacuum conditions. Third, the ions gradually grew to form nanoparticles during the solvothermal process. Finally, the precursors were exfoliated into nanosheets by heat treatment with small-sized CeO_2 uniformly loaded on them. The morphology of the as-synthesized CeO_2/C_3N_4 composites was characterized with SEM and TEM. As shown in Fig. 1b, c, C_3N_4 exhibits a unique layered structure with nanopores. Under vacuum, cerium ions, ethanol, and ethylene glycol enter the interlayer of the hexagonal layered rod precursor (Fig. S1) synthesized by self-assembly of melamine. The interlayer force of the precursor is destroyed during heat treatment, and finally, it is exfoliated into nanosheets. Nanopore formation is due to the release of gas during heat treatment. Furthermore, CeO_2 nanoparticles with an average size of 18.8 nm (Fig. S2) can be recognized in TEM images as uniformly dispersed on the C_3N_4 nanosheets (Fig. 1d–f). The lattice spacing of the CeO_2 nanoparticles is 0.31 nm (Fig. 1f), corresponding to the (111) crystal plane of CeO_2. The scanning TEM (STEM) image (Fig. 1g) and energy dispersive X-ray (EDX) mapping images (Fig. 1h–k) of CeO_2/C_3N_4 clearly exhibit uniformly distributed C, N, O, and Ce elements, suggesting the coexistence of CeO_2 and C_3N_4 in the composites. These results demonstrate the successful synthesis of CeO_2/C_3N_4 composites. The AFM image shows that the thickness of CeO_2/C_3N_4 is approximately 5 nm (Fig. S3), revealing the ultrathin structure of C_3N_4 nanosheets. In comparison, CeO_2/BCN was synthesized by using BCN instead of the precursor. The SEM image shows only BCN with aggregated CeO_2 of approximately 500 nm distributed on it (Fig. S4). The SEM image of the CeO_2/C_3N_4 composite prepared without vacuum assistance (Fig. S5) shows separated C_3N_4 nanosheets and aggregated CeO_2 particles with a size of 200–500 nm, which proves that the vacuum-assisted intercalation strategy is crucial for the heterojunction synthesis. These results prove that the *in situ* intercalation strategy is effective for efficiently exfoliating C_3N_4 and successfully dispersing CeO_2 to prepare the composites with intimate contact, which benefits the charge separation and transfer.

To further certify the structure and composition, powder XRD and FT-IR spectroscopy were applied. As shown in Fig. 2a, the CeO_2, CeO_2/C_3N_4, and CeO_2/BCN samples exhibit the characteristic diffraction peaks at 2θ of 28.5°, 33.1°, 47.5°, and 56.3°, corresponding to the (111), (200), (220), and (311) crystal planes

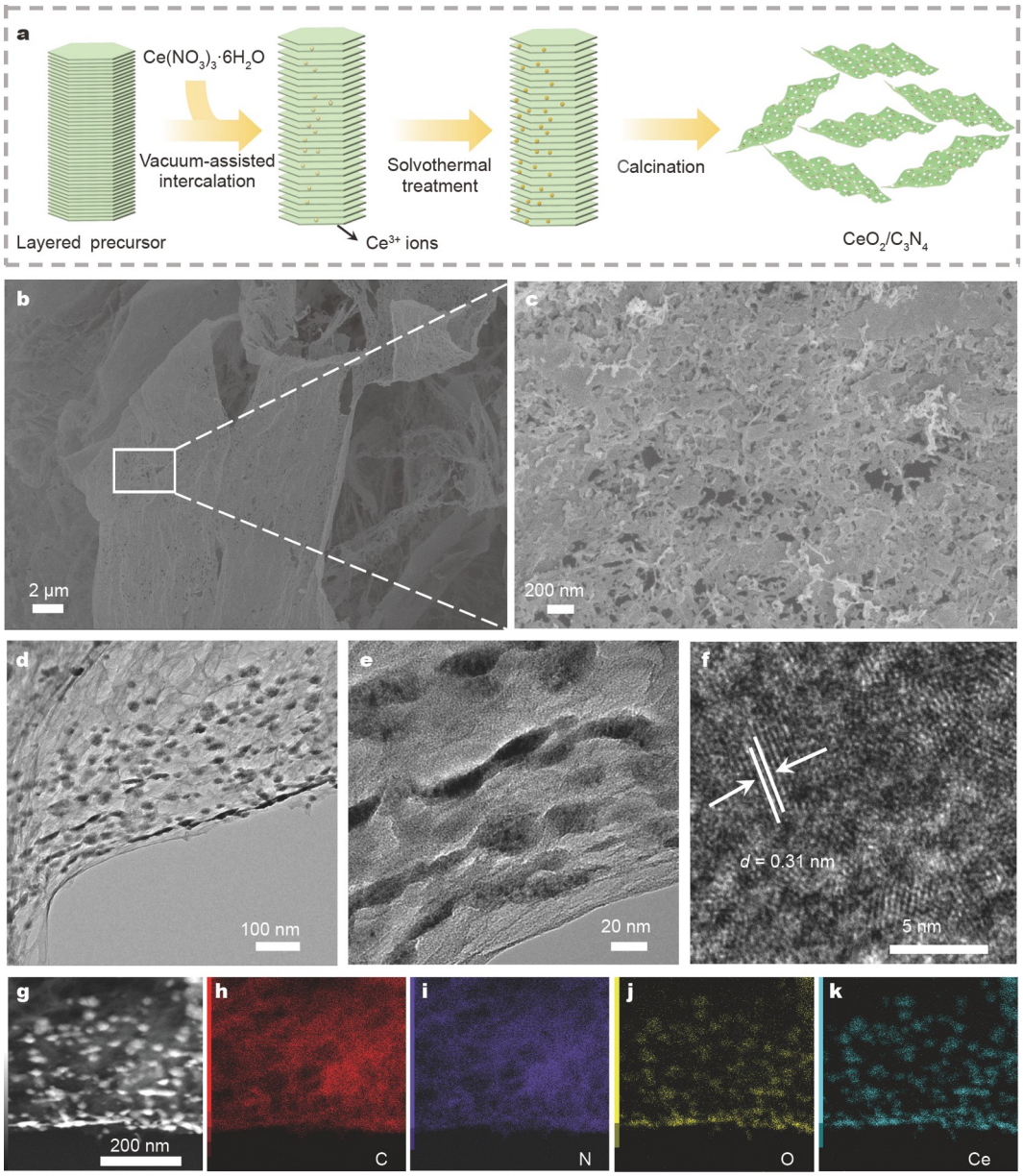

Figure 1 (a) Schematic of the synthesis of the CeO_2/C_3N_4 heterojunction. (b, c) SEM images of CeO_2/C_3N_4. (d–f) TEM and high-resolution TEM (HR-TEM) images of CeO_2/C_3N_4. (g) High-angle annular dark-field-STEM (HAADF-STEM) image of CeO_2/C_3N_4 and (h–k) the corresponding EDX mapping images of elemental C, N, O, and Ce.

of CeO_2 (JCPDS no. 34-0394), respectively [37]. In addition, diffraction peaks at 13.7° and 27.8° are observed in CeO_2/BCN and pristine BCN, corresponding to the (100) and (002) crystal planes of C_3N_4, respectively. Compared with that of CeO_2/BCN, the diffraction peak of CeO_2/C_3N_4 at 13.7° is not obvious, and the peak at 27.8° is broader, indicating the formation of a 2D porous sheet structure of CeO_2/C_3N_4 [38].

The above results indicate the successful exfoliation of BCN and the combination of the two compounds, consistent with the results from FT-IR spectroscopy. As shown in Fig. 2b, for pure C_3N_4, three strong characteristic vibrational peaks are observed. Typically, the peak at 804 cm^{-1} is attributed to the bending vibration of the heptazine rings on C_3N_4. The vibration peaks from 1200 to 1700 cm^{-1} are related to the stretching of aromatic C–N, corresponding to the typical C–N, and C=N heterocyclic skeleton. The broad peak located at 3500–3000 cm^{-1} is attributed to the physically absorbed water molecules and amino ($-NH_2$) groups [39]. The spectra of CeO_2/C_3N_4 and CeO_2/BCN give similar IR signals to pure C_3N_4, but the peak in the 3500–3000 cm^{-1} range is wider and has a slight redshift because of the hydrogen bond between CeO_2 and C_3N_4 [40]. Hydrogen bonding can further promote electron transfer between two species [41]. Moreover, the contents of C_3N_4 and CeO_2 in the synthesized composites were evaluated with the TG. As an organic compound, C_3N_4 completely decomposes with increasing temperature, while CeO_2 eventually remains as CeO_2. Therefore, the mass ratio of CeO_2 in the CeO_2/C_3N_4 composite was confirmed to be 5.3% (Fig. S6).

Nitrogen adsorption-desorption measurements were taken to investigate the textural and structural properties of the as-acquired catalysts. The N_2 adsorption-desorption isotherms of CeO_2/C_3N_4, CeO_2/BCN, CeO_2, and BCN are displayed in Fig. 2c.

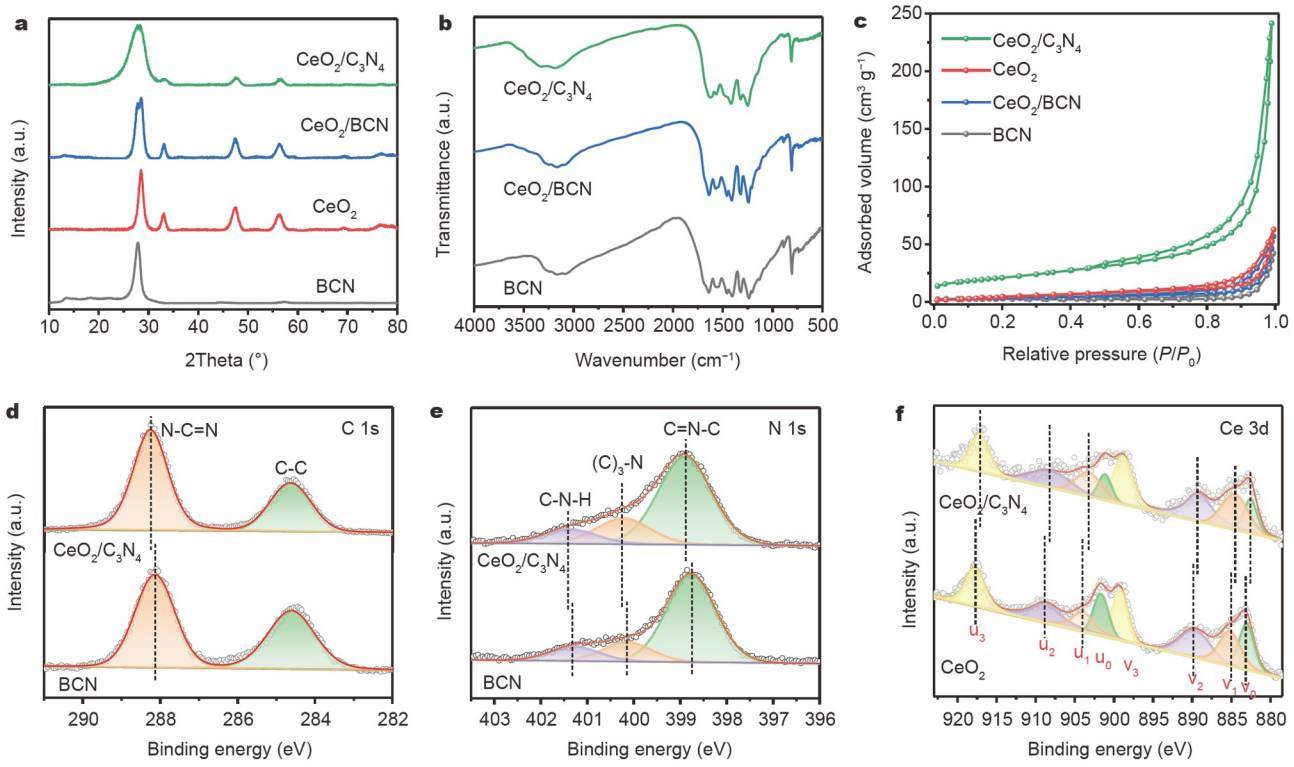

Figure 2 (a) XRD patterns of CeO_2/C_3N_4, CeO_2/BCN, CeO_2, and BCN. (b) FT-IR spectra of CeO_2/C_3N_4, CeO_2/BCN, and CeO_2. (c) Nitrogen adsorption-desorption isotherms of CeO_2/C_3N_4, CeO_2/BCN, CeO_2, and BCN. (d) C 1s and (e) N 1s XPS spectra of CeO_2/C_3N_4 and BCN. (f) Ce 3d XPS spectra of CeO_2/C_3N_4 and CeO_2.

The specific surface area of the sample can be obtained from Brunauer-Emmett-Teller analysis. CeO_2/C_3N_4 has the largest specific surface area (74.9 $m^2 g^{-1}$), which is approximately 3.7 times that of CeO_2 (20.2 $m^2 g^{-1}$), 6.0 times that of CeO_2/BCN (12.5 $m^2 g^{-1}$), and 8.9 times that of BCN (8.4 $m^2 g^{-1}$). The larger surface area of the CeO_2/C_3N_4 heterojunction photocatalyst might provide more catalytically active reaction sites and promote CO_2 adsorption to improve the photocatalytic performance [42].

To investigate the surface structure and interaction between CeO_2 and C_3N_4 of CeO_2/C_3N_4, XPS analysis was performed. As shown in Fig. S7a, the survey spectra of CeO_2/C_3N_4 further indicate the presence of C, N, O, and Ce elements, suggesting that the heterostructure is obtained. The C 1s spectrum (Fig. 2d) shows the characteristic peaks of C_3N_4 at 284.61 and 288.14 eV, which can be attributed to the C–C, and N–C=N groups, respectively [43]. Notably, the N–C=N groups of CeO_2/C_3N_4 are shifted toward a higher binding energy compared with pure C_3N_4, indicating partial electron transfer from C_3N_4 to CeO_2 [44]. The electron transfer is also indicated by the N 1s spectrum (Fig. 2e). The N 1s spectrum of CeO_2/C_3N_4 can be deconvoluted into three main peaks at 398.90, 400.23, and 401.38 eV, corresponding to sp^2-hybridized C=N–C, tricoordinated ($(C)_3$–N) nitrogen atoms, and amino (C–N–H) groups, respectively [45,46]. Correspondingly, the peaks of N 1s in CeO_2/C_3N_4 are also shifted slightly toward higher binding energies compared with those of pure C_3N_4. Furthermore, the Ce 3d peaks can be fitted into eight peaks labeled as v_0 (882.54 eV), v_1 (884.55 eV), v_2 (889.15 eV), v_3 (898.82 eV), u_0 (901.14 eV), u_1 (903.24 eV), u_2 (908.05 eV), and u_3 (917.18 eV) (Fig. 2f). Four of these peaks, u_0, u_1, u_2, and u_3, can be attributed to Ce $3d_{3/2}$, while the other four peaks can be assigned to Ce $3d_{5/2}$ [47]. In addition, v_1 and u_1 are consistent with the features of the Ce^{3+} 3d state, and the other six peaks indicate the presence of Ce^{4+} ions [48]. Thus, the Ce^{4+} and Ce^{3+} species coexist on CeO_2 and CeO_2/C_3N_4 surfaces.

In addition, the EPR spectrum of CeO_2 in Fig. S8 shows two paramagnetic signals (g_I = 1.96 and g_{II} = 1.94), which also support the presence of Ce^{3+} [49]. Fig. 2f shows that the proportion of $Ce^{3+}/(Ce^{3+} + Ce^{4+})$ (26.5%) in CeO_2/C_3N_4 is higher than that of pure CeO_2 (23.3%). The higher proportion of Ce^{3+} indicates an increased content of oxygen vacancies in the material, which benefits the charge transfer and performance improvement [50,51]. Moreover, compared with the pristine CeO_2, the binding energies of Ce 3d in CeO_2/C_3N_4 are slightly shifted to lower energies, which is caused by the partial electron transfer from C_3N_4 to CeO_2. Three diffraction peaks at 529.64, 531.4, and 532.67 eV are observed in the O 1s spectrum (Fig. S7b), corresponding to lattice oxygen (O_L), chemisorbed oxygen or/and weakly bonded oxygen species (O_C), and surface-adsorbed oxygen species, respectively [52]. CeO_2/C_3N_4 has lower O_L content; thus, it contains more oxygen defects. In addition, the O_L peak of CeO_2/C_3N_4 is shifted to higher binding energy because the formation of oxygen defects decreases the electron density of lattice oxygens, and the other two peaks shift toward lower binding energies due to the charge transfer between species [53]. The above XPS results prove that after the combination, the electrons on CeO_2 transfer to C_3N_4, forming an internal electric field directed from C_3N_4 to CeO_2 near the interface. The strong interfacial coupling effect between C_3N_4 and CeO_2 can promote the separation and transfer of photogenerated carriers and further improve CeO_2/C_3N_4 photocatalytic performance. In addition, no characteristic peak of the P element was found in

the P 2p spectrum (Fig. S7c), indicating that adsorbed P species were completely removed through multiple washing with water.

Band structure and photogenerated charge transfer

The optical properties and band structure of the samples can be recognized by UV-vis solid DRS and VB XPS spectra. The absorption edges of the two heterojunction materials clearly exhibit slight blueshift compared with pure C_3N_4 (Fig. 3a), and CeO_2/C_3N_4 has an obvious absorption in the visible range, which is more conducive to the generation of photogenerated carriers. The corresponding band gaps of BCN and CeO_2 are estimated to be 2.70 and 2.87 eV, respectively (Fig. 3b). Notably, C_3N_4 has marginal absorption of visible light because of the electron transition from the VB of N_{2p} orbitals to the CB of C_{2p} orbitals. The VB positions can be obtained from VB XPS (Fig. 3c). The VB positions of pure CeO_2 and pure BCN can be estimated as 2.42 and 1.67 eV, respectively. Thus, the CB edges are calculated according to the corresponding band gap and VB band values to be −1.03 and −0.45 eV for pure BCN and pure CeO_2, respectively. Further, we conducted the Mott-Schottky test of BCN and CeO_2 at three frequencies (Fig. S9), and the CB positions were determined to be −1.01 and −0.49 eV, respectively, consistent with the calculated results using the corresponding band gap and VB band values. The more positive the VB of CeO_2 is, the more negative the CB of C_3N_4, and the interlaced energy-level structure between them is more conducive to the formation of an efficient Z-type charge transfer system.

The changes in the material morphology and electronic structure not only affect the band gap structure of the materials but also substantially inhibit the recombination of photogenerated carriers. Steady-state and time-resolved PL spectroscopy was used to reveal the photophysical properties of photogenerated electron holes. According to the steady-state PL spectra (Fig. 3d), the peak intensity of CeO_2/C_3N_4 is considerably lower than that of CeO_2/BCN and BCN, which indicates that its electron-hole recombination rate is effectively inhibited. Subsequently, time-resolved fluorescence spectra were obtained, and the results are shown in Fig. S10. The corresponding fluorescence lifetime results show that the CeO_2/C_3N_4 heterojunction has the longest lifetime of 7.3 ns, indicating that the charge separation efficiency has been improved by constructing the CeO_2/C_3N_4 heterojunction structure.

Photoelectrochemical measurements were performed to further investigate the mechanism of the photocatalytic activity of the composites. Transient photocurrent response is a useful technique for studying the separation efficiency of photogenerated electron-hole pairs and further evaluating the performance of charge carrier generation and transfer in reactive systems. As is well known, the photocurrent largely depends on the number of photogenerated electrons, and the greater the number of generated electrons is, the greater the photocurrent density. As shown in Fig. 3e, the saturation photocurrent densities remain constant when the light is turned on and decrease immediately once the light is turned off. Notably, the photocurrent response of CeO_2/C_3N_4 is approximately 5-, 4-, and 2-fold higher than those of CeO_2, BCN and CeO_2/BCN, which denotes that CeO_2/C_3N_4 has a more efficient separation and longer lifetime of photogenerated electron-hole pairs. The enhanced photocurrent of CeO_2/C_3N_4 indicates a higher separation efficiency of photogenerated electrons and holes, which is due to the interaction of C_3N_4 and CeO_2. In addition, Fig. 3f shows the electrochemical impedance spectra (EIS) of the photocatalysts. In each case, only one arc/semicircle can be observed on the EIS plane. The arc radius of the EIS Nyquist plot

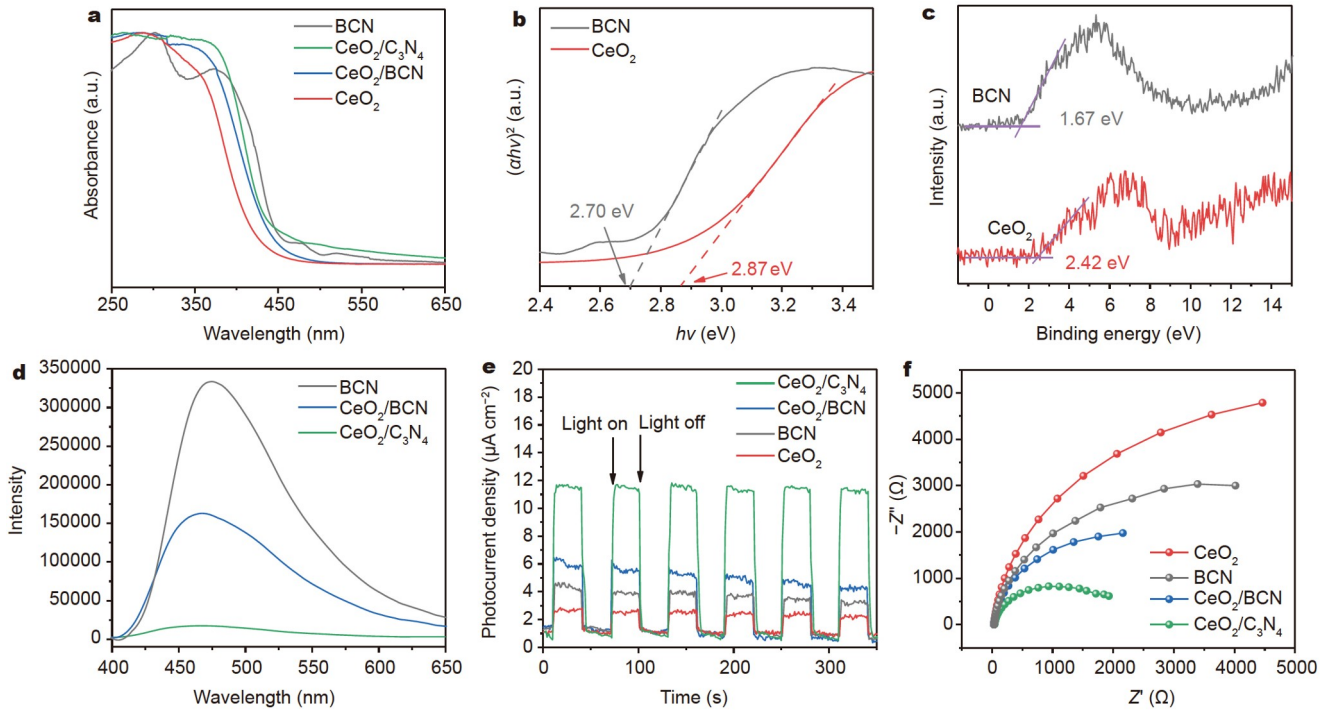

Figure 3 (a) UV-vis DRS spectra of CeO_2/C_3N_4, CeO_2/BCN, CeO_2, and BCN. (b) Corresponding plots of $(\alpha h\nu)^2$ *versus* photon energy ($h\nu$). (c) VB XPS spectra of BCN and CeO_2. (d) Steady-state PL spectra of CeO_2/C_3N_4, CeO_2/BCN, and BCN (365 nm excitation). (e) Transient photocurrent response of CeO_2/C_3N_4, CeO_2/BCN, CeO_2, and BCN with repeated on-off cycles under simulated sunlight irradiation. (f) Nyquist plots of EIS for CeO_2/C_3N_4, CeO_2/BCN, CeO_2, and BCN.

reflects the reaction rate at the electrode surface. It is much smaller for the CeO_2/C_3N_4 electrode than for BCN, CeO_2, and CeO_2/BCN, indicating rapid interfacial charge transfer and effective separation of photogenerated electron-hole pairs. In this respect, these results agree well with the photocurrent measurements. Moreover, the linear sweep voltammetry (LSV) results of CeO_2, BCN, CeO_2/BCN, and CeO_2/C_3N_4 are shown in Fig. S11. The CeO_2/C_3N_4 composite has the highest current density under identical voltage conditions; thus, the photogenerated carrier density inside this catalyst is higher than that of other samples under the same light intensity. These excellent optoelectronic properties of CeO_2/C_3N_4 indicate its efficient charge carrier generation and transfer under photoemission, which is crucial for excellent CO_2 photoreduction performance.

Photocatalytic performance

The CO_2 photocatalytic reduction reaction performance of different samples was evaluated without a noble metal cocatalyst or a sacrificial agent. Fig. 4a, b exhibit the time-dependent CO and CH_4 yields for different catalysts under full light irradiation. Pure BCN and pure CeO_2 exhibit relatively low production rates of CO (7.16 and 5.48 μmol g^{-1} in 4 h) and CH_4 (0.64 and 0.20 μmol g^{-1} in 4 h), resulting from the rapid charge recombination. Compared with pure CeO_2 and pure BCN, CeO_2/C_3N_4 and CeO_2/BCN show improved photocatalytic performance, indicating that the heterostructure plays an important role in promoting electron-hole separation for an improvement in photocatalytic performance. CeO_2/C_3N_4 exhibits the highest photocatalytic CO_2 reduction performance with 35.96 μmol g^{-1} of CO, which is approximately 5-, 6.5-, and 2-fold larger than

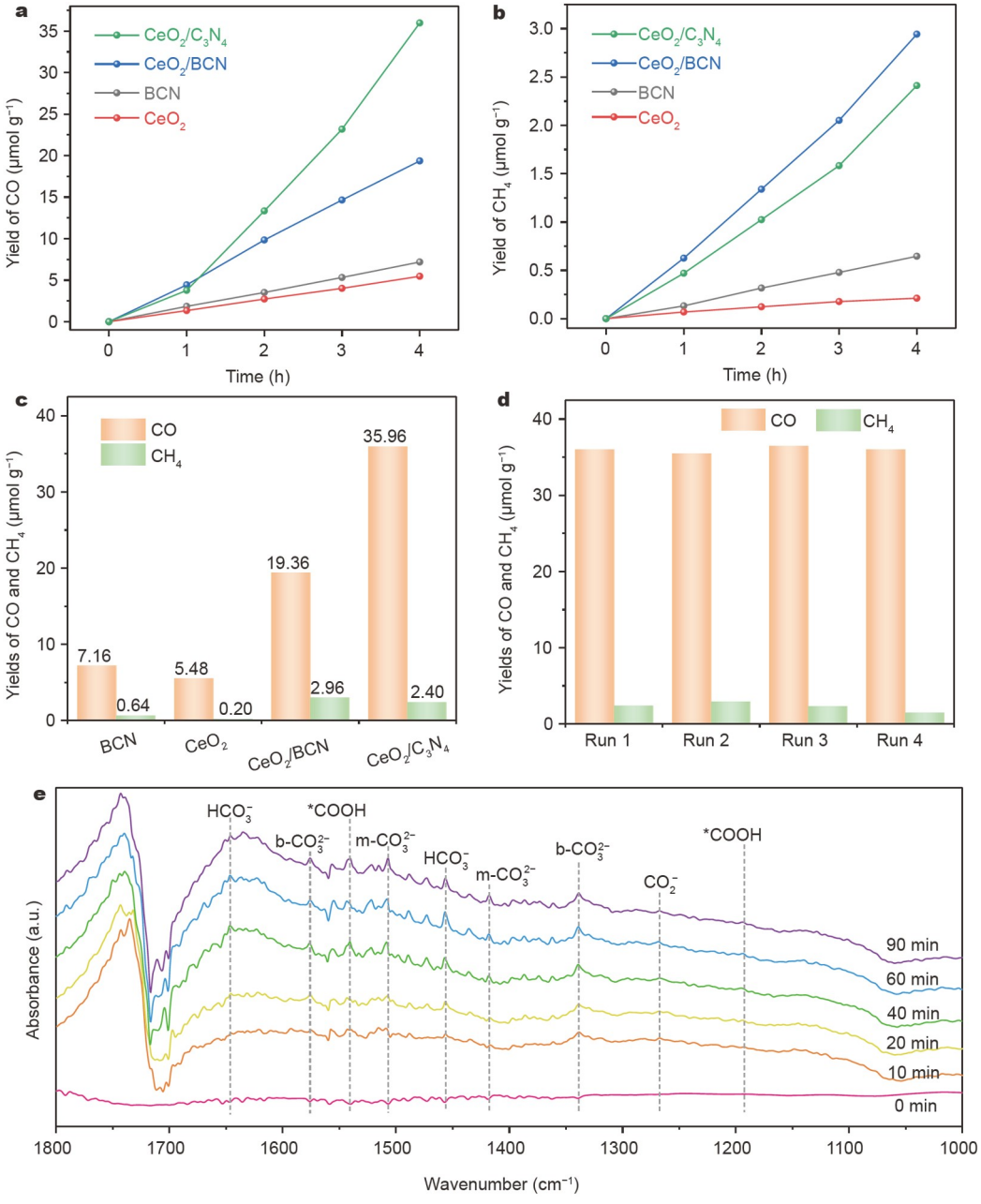

Figure 4 (a) Time courses of photocatalytic CO evolutions. (b) Time courses of photocatalytic CH_4 evolutions. (c) Photocatalytic CO_2 reduction activities of BCN, CeO_2, CeO_2/BCN, and CeO_2/C_3N_4 for 4 h. (d) Four-cycle experimental diagram of CeO_2/C_3N_4 photocatalyst. (e) *In situ* DRIFT spectra of CeO_2/C_3N_4.

those of BCN, CeO_2, and CeO_2/BCN, respectively, with the CH_4 yield of 2.40 μmol g^{-1} for 4 h. This enhanced performance is caused by the increased specific surface area, CO_2 adsorption, and the effective separation of photogenerated carriers.

Generally, the photocatalytic reduction efficiency of CO_2 mainly depends on the adsorption and activation of CO_2, the light absorption capacity, and the charge transfer capacity of the catalyst. The adsorption and activation of CO_2 is the first step in the reduction reaction. CeO_2/C_3N_4 contains numerous oxygen defects, which can make CO_2 molecules combine with the surface of the catalyst through chemical bonds, which is conducive to further reactions [54]. In addition, the larger specific surface area of the lamellar structure can increase the adsorption capacity of CO_2 and provide more active sites. Moreover, the construction of the Z-scheme heterojunction has good interfacial activity and can improve charge separation efficiency. Control experiments show that no CO or CH_4 was detected in the absence of photocatalysts or light irradiation, indicating that these components are necessary for the current gaseous photocatalytic CO_2 reduction process. In addition, experiments were performed by replacing CO_2 with Ar, and no obvious reduction products were detected. This result also proves that CO_2 is the only carbon source. Fig. 4d shows the cycling stability experimental results of CeO_2/C_3N_4. The photocatalytic performance of CeO_2/C_3N_4 has no obvious attenuation after four cycles, indicating the excellent photostability of the CeO_2/C_3N_4 hybrid and its potential for long-term photocatalytic applications.

To better understand the photoreduction process, the *in situ* DRIFT spectroscopy of CeO_2/C_3N_4 was used to characterize the adsorbed species and key intermediates during the reaction. As shown in Fig. 4e, in the range of 1000–1750 cm^{-1}, nine main characteristic absorption peaks are observed. All peaks increased with the irradiation time. The peaks that appeared near 1268, 1457, and 1646 cm^{-1} indicated the presence of carboxylate (CO_2^-) and hydrocarboxylate (HCO_3^-) species, respectively [55]. The peaks at 1418, 1507, 1339, and 1576 cm^{-1} are due to the groups of monodentate carbonate (m-CO_3^{2-}) and bidentate carbonate (b-CO_3^{2-}), respectively [56]. *COOH, which is generally considered the main intermediate of CO formation, is observed at 1194 and 1541 cm^{-1} [57,58]. However, no obvious peaks of active species that can generate CH_4 are observed. These observations show that the adsorbed CO_2 molecules are more often converted into CO, and less CH_4 is generated, consistent with the experimental results.

Proposed mechanism of CO_2 photoreduction

To further study the enhanced CO_2 photoreduction performance of CeO_2/C_3N_4, EPR spectroscopy was used to analyze the electron transfer direction in the system. The experiment was performed at room temperature. 5,5-Dimethyl-1-pyrroline *N*-oxide (DMPO) was used as the spin-trapping reagent. The characteristic peaks of active superoxide ($\bullet O_2^-$) species and hydroxyl ($\bullet$OH) radicals of C_3N_4, CeO_2, and CeO_2/C_3N_4 composites are shown in Fig. 5a, b. As displayed in Fig. 5a, a 1:1:1:1 electron spin resonance spectrum signal corresponding to the DMPO-$\bullet O_2^-$ characteristic peak is observed in the C_3N_4 and CeO_2/C_3N_4 composites, but no obvious signal is observed in CeO_2. Notably, for the CeO_2/C_3N_4 composites, the signal intensity of the $\bullet O_2^-$ characteristic peak is stronger than that of C_3N_4. For CeO_2 and CeO_2/C_3N_4 composites, four obvious characteristic peaks with

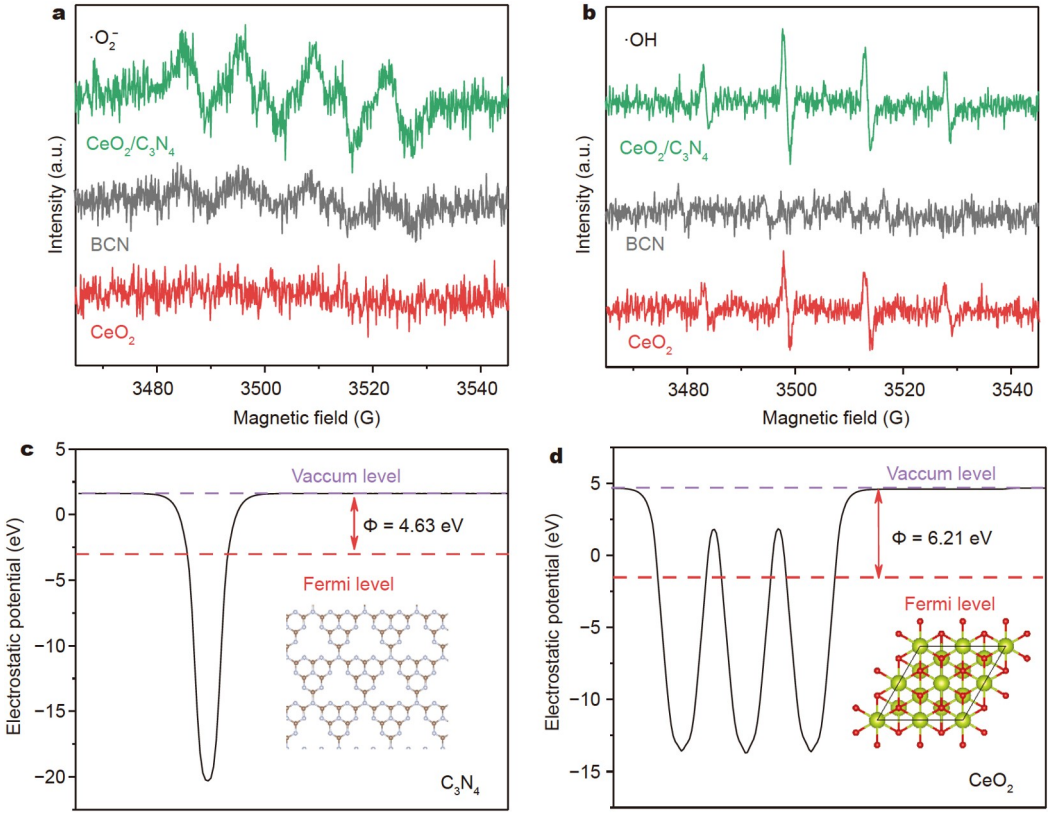

Figure 5 DMPO spin-trapping EPR spectra of (a) DMPO-$\bullet O_2^-$ and (b) DMPO-$\bullet$OH of CeO_2/C_3N_4, BCN, and CeO_2. Calculated work functions and top view of (c) C_3N_4 and (d) CeO_2.

an intensity near 1:2:2:1 are observed, indicating that the signal is due to DMPO-•OH, and no corresponding EPR signal is observed in C_3N_4. Similarly, the •OH signal of the CeO_2/C_3N_4 composite is stronger than that of CeO_2. All the above trapping conclusions indicate that the prepared hybrid follows the Z-scheme system rather than the traditional type-II heterojunction structure. Furthermore, the EPR spectrum signal intensity of CeO_2/C_3N_4 is stronger than that of a single semiconductor, which is caused by the retained photogenerated electrons and holes with stronger reduction ability and the oxidation ability of the Z-scheme heterojunction.

DFT calculations were used to directly explain the interfacial charge transfer between C_3N_4 and CeO_2. As shown in Fig. 5c, d, the calculated work functions of the C_3N_4 (001) and CeO_2 (111) surfaces are 4.63 and 6.21 eV, respectively, indicating that charge transfer can occur at the interface between C_3N_4 and CeO_2. The work function of C_3N_4 is more negative than that of CeO_2, indicating that the electrons of C_3N_4 can spontaneously flow into CeO_2 through the CeO_2/C_3N_4 heterostructure interface until the equivalent Fermi level is obtained. The electron transfer then creates an internal electric field. Therefore, C_3N_4 is positively charged at the interface, while CeO_2 is negatively charged. This result is consistent with the XPS measurement result. We also tested the work functions of C_3N_4, CeO_2, and CeO_2/C_3N_4 through a Kelvin probe (Fig. S12), and the results obtained are almost consistent with the theoretical calculation results.

On the basis of the above experimental results, we propose the band structure and electron migration path before and after CeO_2 and C_3N_4 contact (Fig. 6). Particularly, the initial Fermi energy level of C_3N_4 is higher than that of CeO_2. When the CeO_2 particles are tightly bound on the C_3N_4 surface, electrons flow spontaneously from C_3N_4 to CeO_2 until their Fermi energy levels are aligned. Therefore, the edge of the energy band is bent at the interface, and an internal electric field from C_3N_4 to CeO_2 is generated at the interface. Under simulated sunlight illumination, CeO_2 and C_3N_4 are excited to generate electrons (e^-) and holes (h^+). Therefore, driven by the internal electric field at the interface of the CeO_2/C_3N_4 heterojunction, the excited electrons in the CeO_2 CB are transferred to the interface and combine with the photoinduced holes in the C_3N_4 VB, thus maintaining the strong reducibility of electrons in the C_3N_4 CB and the strong oxidation of holes in the CeO_2 VB. Photogenerated electrons accumulated on the C_3N_4 surface facilitate photoreaction. The CO_2 molecules adsorbed on the catalyst capture these electrons and then react with protons to generate CH_4 and CO [59]. At the same time, the holes left on the CeO_2 VB will oxidize water into oxygen, thereby completing the photocatalytic reduction of CO_2.

Therefore, the CeO_2/C_3N_4 Z-scheme heterostructure can achieve efficient separation of photogenerated carriers compared with single-component catalytic materials. Because of these unique properties, CeO_2/C_3N_4 can effectively enhance the photocatalysis of CO_2 to CO and CH_4 under simulated illumination. Furthermore, the prepared CeO_2/C_3N_4 composite can not only achieve strong interface interaction through the close combination between CeO_2 and C_3N_4 but also establish an effective interface electronic effect. In addition, the CeO_2/C_3N_4 heterojunction has a large specific surface area, which increases the contact area between the active site and CO_2, thereby increasing the amount of adsorbed CO_2. Meanwhile, the presence of oxygen vacancies on CeO_2 also promotes the adsorption of CO_2 [60].

CONCLUSIONS

In this work, Z-scheme heterostructures with CeO_2 nanoparticles uniformly loaded on ultrathin porous C_3N_4 nanosheets were designed and fabricated by using an *in situ* exfoliation and conversion approach. The CeO_2/C_3N_4 composite possesses improved photocatalytic performance in photocatalytic CO_2 reduction, with an evolution rate of 35.96 μmol g^{-1} for CO and 2.40 μmol g^{-1} for CH_4 in 4 h without a noble metal cocatalyst or a sacrificial agent, which is an approximately 5-fold photoactivity improvement compared with that of BCN. The improved performance of CeO_2/C_3N_4 hierarchical composites is mainly due to synergism between the following advantages: (1) the ultrathin porous nanosheets can not only increase the specific surface area to provide more active sites but also effectively shorten the migration distance of photogenerated electron holes to reduce the possibility of their recombination; (2) the construction of CeO_2/C_3N_4 heterojunctions with intimate interface contact can effectively promote the separation and transfer of photogenerated carriers; (3) the well-matched band gaps of CeO_2 and C_3N_4 induce the Z-scheme structure, which has good ability of light collection and utilization and can separate the active sites in space to achieve strong redox ability. Our study exemplifies the artificial construction of a direct Z-scheme ultrathin C_3N_4-based photocatalyst and can help to broaden its application. In the future, constructing more C_3N_4-

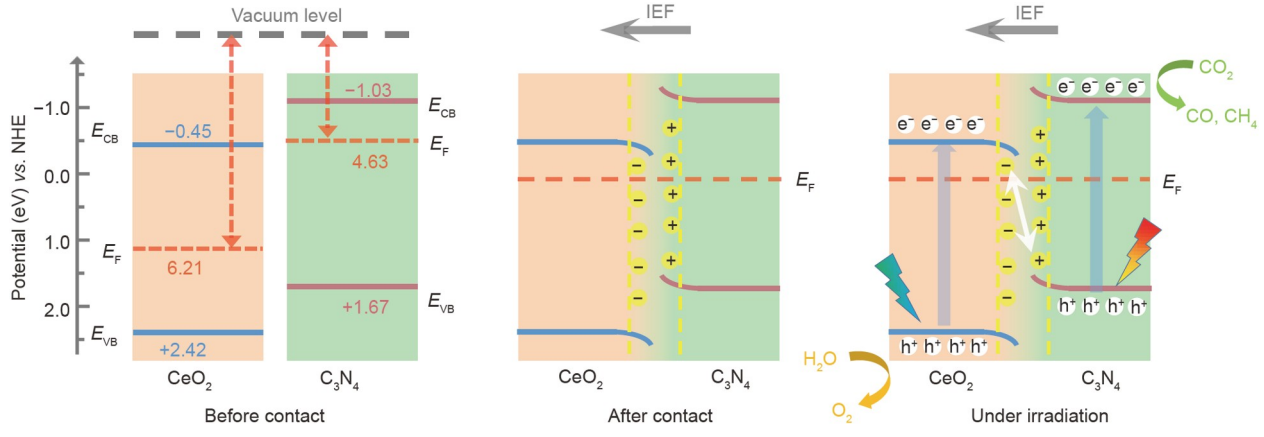

Figure 6 Schematic of the Z-scheme charge transfer process and photocatalytic reaction mechanism of CeO_2/C_3N_4 under light irradiation.

based direct Z-scheme photocatalysts with matched band alignments and intimate interfaces will be crucial for expanding the potential use of photocatalysts in various applications. By adjusting the position of the energy band through heterojunction construction, photocatalysts with suitable band structures can be designed for dual simultaneous redox reactions for the production of value-added chemicals. Moreover, because of their low cost, high yield, and environmental friendliness, C_3N_4-based photocatalysts can also be developed to treat contaminated drinking water and wastewater containing hazardous or non-biodegradable compounds. Finally, because of their outstanding biocompatibility and the low biological toxicity of C_3N_4, the application of these photocatalysts in the field of biomedicine (e.g., magnetic resonance imaging and photodynamic therapy) is highly promising.

Received 23 January 2023; accepted 3 March 2023; published online 30 May 2023

1 Qian C, Sun W, Hung DLH, *et al.* Catalytic CO_2 reduction by palladium-decorated silicon-hydride nanosheets. Nat Catal, 2018, 2: 46–54
2 Chang X, Wang T, Yang P, *et al.* The development of cocatalysts for photoelectrochemical CO_2 reduction. Adv Mater, 2019, 31: 1804710
3 Fu J, Jiang K, Qiu X, *et al.* Product selectivity of photocatalytic CO_2 reduction reactions. Mater Today, 2020, 32: 222–243
4 Jiang Z, Sun H, Wang T, *et al.* Nature-based catalyst for visible-light-driven photocatalytic CO_2 reduction. Energy Environ Sci, 2018, 11: 2382–2389
5 Wan L, Zhou Q, Wang X, *et al.* Cu_2O nanocubes with mixed oxidation-state facets for (photo)catalytic hydrogenation of carbon dioxide. Nat Catal, 2019, 2: 889–898
6 Cai M, Wu Z, Li Z, *et al.* Greenhouse-inspired supra-photothermal CO_2 catalysis. Nat Energy, 2021, 6: 807–814
7 Yi L, Zhao W, Huang Y, *et al.* Tungsten bronze $Cs_{0.33}WO_3$ nanorods modified by molybdenum for improved photocatalytic CO_2 reduction directly from air. Sci China Mater, 2020, 63: 2206–2214
8 Xia P, Antonietti M, Zhu B, *et al.* Designing defective crystalline carbon nitride to enable selective CO_2 photoreduction in the gas phase. Adv Funct Mater, 2019, 29: 1900093
9 Yin S, Zhao X, Jiang E, *et al.* Boosting water decomposition by sulfur vacancies for efficient CO_2 photoreduction. Energy Environ Sci, 2022, 15: 1556–1562
10 Al-Ahmed A. Photocatalytic properties of graphitic carbon nitrides (g-C_3N_4) for sustainable green hydrogen production: Recent advancement. Fuel, 2022, 316: 123381
11 Wu B, Zhang L, Jiang B, *et al.* Ultrathin porous carbon nitride bundles with an adjustable energy band structure toward simultaneous solar photocatalytic water splitting and selective phenylcarbinol oxidation. Angew Chem Int Ed, 2021, 60: 4815–4822
12 Xiao X, Gao Y, Zhang L, *et al.* A promoted charge separation/transfer system from Cu single atoms and C_3N_4 layers for efficient photocatalysis. Adv Mater, 2020, 32: 2003082
13 Yang B, Wang Z, Zhao J, *et al.* 1D/2D carbon-doped nanowire/ultrathin nanosheet g-C_3N_4 isotype heterojunction for effective and durable photocatalytic H_2 evolution. Int J Hydrogen Energy, 2021, 46: 25436–25447
14 Hou H, Zeng X, Zhang X. 2D/2D heterostructured photocatalyst: Rational design for energy and environmental applications. Sci China Mater, 2020, 63: 2119–2152
15 Wang N, Wang D, Wu A, *et al.* Few-layered MoS_2 anchored on 2D porous C_3N_4 nanosheets for Pt-free photocatalytic hydrogen evolution. Nano Res, 2023, 16: 3524–3535
16 Xiao Y, Guo S, Tian G, *et al.* Synergetic enhancement of surface reactions and charge separation over holey C_3N_4/TiO_2 2D heterojunctions. Sci Bull, 2021, 66: 275–283
17 Fu J, Yu J, Jiang C, *et al.* g-C_3N_4-based heterostructured photocatalysts. Adv Energy Mater, 2018, 8: 1701503
18 Chen X, Chen Y, Liu X, *et al.* Boosted charge transfer and photocatalytic CO_2 reduction over sulfur-doped C_3N_4 porous nanosheets with embedded SnS_2-SnO_2 nanojunctions. Sci China Mater, 2021, 65: 400–412
19 Sohail M, Anwar U, Taha TA, *et al.* Nanostructured materials based on g-C_3N_4 for enhanced photocatalytic activity and potentials application: A review. Arabian J Chem, 2022, 15: 104070
20 Li YY, Zhou BX, Zhang HW, *et al.* A host-guest self-assembly strategy to enhance π-electron densities in ultrathin porous carbon nitride nanocages toward highly efficient hydrogen evolution. Chem Eng J, 2022, 430: 132880
21 Li B, Tian Z, Li L, *et al.* Directional charge transfer channels in a monolithically integrated electrode for photoassisted overall water splitting. ACS Nano, 2023, 17: 3465–3482
22 Li B, Peng W, Zhang J, *et al.* High-throughput one-photon excitation pathway in 0D/3D heterojunctions for visible-light driven hydrogen evolution. Adv Funct Mater, 2021, 31: 2100816
23 Li X, Hu J, Yang T, *et al.* Efficient photocatalytic H_2-evolution coupled with valuable furfural-production on exquisite 2D/2D $LaVO_4$/g-C_3N_4 heterostructure. Nano Energy, 2022, 92: 106714
24 Shao B, Liu X, Liu Z, *et al.* Synthesis and characterization of 2D/0D g-C_3N_4/CdS-nitrogen doped hollow carbon spheres (NHCs) composites with enhanced visible light photodegradation activity for antibiotic. Chem Eng J, 2019, 374: 479–493
25 Hua Q, Zhou X, Zhang B, *et al.* Band modulation and interfacial engineering to generate efficient visible-light-induced bifunctional photocatalysts. ACS Sustain Chem Eng, 2020, 8: 2919–2930
26 Qiao Q, Yang K, Ma LL, *et al.* Facile *in situ* construction of mediator-free direct Z-scheme g-C_3N_4/CeO_2 heterojunctions with highly efficient photocatalytic activity. J Phys D-Appl Phys, 2018, 51: 275302
27 Gao H, Yang H, Xu J, *et al.* Strongly coupled g-C_3N_4 nanosheets-Co_3O_4 quantum dots as 2D/0D heterostructure composite for peroxymonosulfate activation. Small, 2018, 14: 1801353
28 Low J, Jiang C, Cheng B, *et al.* A review of direct Z-scheme photocatalysts. Small Methods, 2017, 1: 1700080
29 Huang D, Chen S, Zeng G, *et al.* Artificial Z-scheme photocatalytic system: What have been done and where to go? Coord Chem Rev, 2019, 385: 44–80
30 Dong YJ, Jiang Y, Liao JF, *et al.* Construction of a ternary WO_3/$CsPbBr_3$/ZIF-67 heterostructure for enhanced photocatalytic carbon dioxide reduction. Sci China Mater, 2022, 65: 1550–1559
31 Xie S, Wang Z, Cheng F, *et al.* Ceria and ceria-based nanostructured materials for photoenergy applications. Nano Energy, 2017, 34: 313–337
32 Melchionna M, Fornasiero P. The role of ceria-based nanostructured materials in energy applications. Mater Today, 2014, 17: 349–357
33 Guo S, Deng Z, Li M, *et al.* Phosphorus-doped carbon nitride tubes with a layered micro-nanostructure for enhanced visible-light photocatalytic hydrogen evolution. Angew Chem Int Ed, 2016, 55: 1830–1834
34 Kresse G, Furthmüller J. Efficient iterative schemes for *ab initio* total-energy calculations using a plane-wave basis set. Phys Rev B, 1996, 54: 11169–11186
35 Perdew JP, Burke K, Ernzerhof M. Generalized gradient approximation made simple. Phys Rev Lett, 1996, 77: 3865–3868
36 Grimme S, Antony J, Ehrlich S, *et al.* A consistent and accurate *ab initio* parametrization of density functional dispersion correction (DFT-D) for the 94 elements H-Pu. J Chem Phys, 2010, 132: 154104
37 Li J, Song S, Long Y, *et al.* Investigating the hybrid-structure-effect of CeO_2-encapsulated Au nanostructures on the transfer coupling of nitrobenzene. Adv Mater, 2018, 30: 1704416
38 Li Y, Yang M, Xing Y, *et al.* Preparation of carbon-rich g-C_3N_4 nanosheets with enhanced visible light utilization for efficient photocatalytic hydrogen production. Small, 2017, 13: 1701552
39 Zou W, Deng B, Hu X, *et al.* Crystal-plane-dependent metal oxide-support interaction in CeO_2/g-C_3N_4 for photocatalytic hydrogen evolution. Appl Catal B-Environ, 2018, 238: 111–118
40 Wei X, Wang X, Pu Y, *et al.* Facile ball-milling synthesis of CeO_2/g-C_3N_4 Z-scheme heterojunction for synergistic adsorption and photodegradation of methylene blue: Characteristics, kinetics, models, and

mechanisms. Chem Eng J, 2021, 420: 127719
41 Lin L, Hou C, Zhang X, *et al.* Highly efficient visible-light driven photocatalytic reduction of CO_2 over g-C_3N_4 nanosheets/tetra(4-carboxyphenyl)porphyrin iron(III) chloride heterogeneous catalysts. Appl Catal B-Environ, 2018, 221: 312–319
42 Sun Z, Fang W, Zhao L, *et al.* g-C_3N_4 foam/Cu_2O QDs with excellent CO_2 adsorption and synergistic catalytic effect for photocatalytic CO_2 reduction. Environ Int, 2019, 130: 104898
43 Wang L, Qi Y, Li H, *et al.* Au/g-C_3N_4 heterostructure sensitized by black phosphorus for full solar spectrum waste-to-hydrogen conversion. Sci China Mater, 2021, 65: 974–984
44 Wang H, Guan J, Li J, *et al.* Fabricated g-C_3N_4/Ag/m-CeO_2 composite photocatalyst for enhanced photoconversion of CO_2. Appl Surf Sci, 2020, 506: 144931
45 Ai M, Zhang JW, Gao R, *et al.* MnO_x-decorated 3D porous C_3N_4 with internal donor-acceptor motifs for efficient photocatalytic hydrogen production. Appl Catal B-Environ, 2019, 256: 117805
46 Li Y, Gu M, Shi T, *et al.* Carbon vacancy in C_3N_4 nanotube: Electronic structure, photocatalysis mechanism and highly enhanced activity. Appl Catal B-Environ, 2020, 262: 118281
47 Li X, Wang M, Wang R, *et al.* A distinctive semiconductor-metalloid heterojunction: Unique electronic structure and enhanced CO_2 photoreduction activity. J Colloid Interface Sci, 2022, 615: 821–830
48 Cong Q, Chen L, Wang X, *et al.* Promotional effect of nitrogen-doping on a ceria unary oxide catalyst with rich oxygen vacancies for selective catalytic reduction of NO with NH_3. Chem Eng J, 2020, 379: 122302
49 Marciniak AA, Alves OC, Appel LG, *et al.* Synthesis of dimethyl carbonate from CO_2 and methanol over CeO_2: Role of copper as dopant and the use of methyl trichloroacetate as dehydrating agent. J Catal, 2019, 371: 88–95
50 Hao Y, Ma Y, Zhang X, *et al.* Unraveling the importance between electronic intensity and oxygen vacancy on photothermocatalytic toluene oxidation over CeO_2. Chem Eng J, 2022, 433: 134619
51 Zhuang G, Chen Y, Zhuang Z, *et al.* Oxygen vacancies in metal oxides: Recent progress towards advanced catalyst design. Sci China Mater, 2020, 63: 2089–2118
52 Wang Y, Wang F, Chen Y, *et al.* Enhanced photocatalytic performance of ordered mesoporous Fe-doped CeO_2 catalysts for the reduction of CO_2 with H_2O under simulated solar irradiation. Appl Catal B-Environ, 2014, 147: 602–609
53 Pu Y, Li W, Cai Y, *et al.* Effects of different treatment atmospheres on CeO_2/g-C_3N_4 photocatalytic CO_2 reduction: Good or bad? Catal Sci Technol, 2021, 11: 2827–2833
54 Jiang D, Wang W, Gao E, *et al.* Highly selective defect-mediated photochemical CO_2 conversion over fluorite ceria under ambient conditions. Chem Commun, 2014, 50: 2005–2007
55 Zhao X, Xu M, Song X, *et al.* Charge separation and transfer activated by covalent bond in UiO-66-NH_2/RGO heterostructure for CO_2 photoreduction. Chem Eng J, 2022, 437: 135210
56 Wang Y, Zhao J, Li Y, *et al.* Selective photocatalytic CO_2 reduction to CH_4 over Pt/In_2O_3: Significant role of hydrogen adatom. Appl Catal B-Environ, 2018, 226: 544–553
57 Shangguan W, Liu Q, Wang Y, *et al.* Molecular-level insight into photocatalytic CO_2 reduction with H_2O over Au nanoparticles by interband transitions. Nat Commun, 2022, 13: 3894
58 Yang P, Zhuzhang H, Wang R, *et al.* Carbon vacancies in a melon polymeric matrix promote photocatalytic carbon dioxide conversion. Angew Chem Int Ed, 2019, 58: 1134–1137
59 Chang X, Wang T, Gong J. CO_2 photo-reduction: Insights into CO_2 activation and reaction on surfaces of photocatalysts. Energy Environ Sci, 2016, 9: 2177–2196
60 Kumar A, Singh P, Khan AAP, *et al.* CO_2 photoreduction into solar fuels *via* vacancy engineered bismuth-based photocatalysts: Selectivity and mechanistic insights. Chem Eng J, 2022, 439: 135563

Acknowledgements This work was supported by the National Key R&D Program of China (2022YFA1503003), the National Natural Science Foundation of China (U20A20250, 21801069 and 91961111), the Natural Science Foundation of Heilongjiang Province (YQ2021B008), the Basic Research Fund of Heilongjiang University in Heilongjiang Province (2022-KYYWF-1036 and 2021-KYYWF-0039), and Heilongjiang University Excellent Youth Foundation.

Author contributions Chen J conducted the synthesis of materials and performed the characterizations and photocatalytic tests. Xiao Y, Wang N and Kang X analyzed partial experimental data. Wang D, Wang C and Jiang Y assisted with the experiments and characterizations. Chen J wrote the paper with support from Liu J and Fu H. All authors contributed to the general discussion.

Conflict of interest The authors declare that they have no conflict of interest.

Supplementary information Supporting data are available in the online version of the paper.

Jie Chen is currently an MSc candidate in inorganic chemistry under the supervision of associate Prof. Jiancong Liu and Prof. Honggang Fu at Heilongjiang University. Her research focuses on novel photocatalytic materials.

Jiancong Liu received her BSc and PhD degrees in 2012 and 2017, respectively, from Jilin University. Then, she joined Heilongjiang University as an assistant professor in 2018. Her interests focus on zeolite-based nanocomposites for hydrogenation catalysis and porous materials with long afterglow luminescence properties.

Honggang Fu received his BSc and MSc degrees in 1984 and 1987, respectively, from Jilin University. He joined Heilongjiang University as an assistant professor in 1988. In 1999, he received a PhD degree from Harbin Institute of Technology. He became a full professor in 2000. His interests focus on oxide-based nanomaterials for solar energy conversion and photocatalysis, carbon-based nanomaterials for energy conversion and storage, and electrocatalysis.

简易合成具有增强电荷转移的Z型CeO_2/C_3N_4异质结用于光催化CO_2还原

陈杰[1], 肖玉婷[2], 汪楠[1], 康鑫[1], 王东旭[1], 王春雁[1], 刘健聪[1*], 姜昱辰[1], 付宏刚[1*]

摘要 利用太阳能将CO_2转化为增值燃料, 对于实现全球碳中和的目标具有重要意义, 而光生电荷的有效分离是提高光催化CO_2还原效率的重要影响因素. 在此, 我们报道了一种简易的原位剥离和转化策略, 将CeO_2纳米颗粒均匀分布在超薄多孔C_3N_4纳米片上, 合成了新型的CeO_2/C_3N_4异质结构. C_3N_4的超薄多孔结构不仅可以增加比表面积以提供更多的活性位点, 还可以有效缩短光生电子空穴的迁移距离以避免复合. 此外, 高度分散的CeO_2与C_3N_4之间具有紧密的界面接触, 使更多的电荷通过界面进行转移. 合成的CeO_2/C_3N_4异质结构具有带隙匹配的Z型结构, 可以有效延长光诱导电荷载流子的寿命并提升光催化剂的氧化还原能力. 与传统块状C_3N_4相比, 合成的CeO_2/C_3N_4异质结在没有贵金属作为助催化剂和没有牺牲剂条件下显示出约5倍的CO_2光还原性能的提升. 这项工作为用于可持续能源转换的直接Z型光催化剂的设计和实际应用提供了一种新策略.

